Available online at www.sciencedirect.com
ScienceDirect
Journal of Solid State Chemistry 181 (2008) 1056–1069
JOURNAL OF SOLID STATE CHEMISTRY
www.elsevier.com/locate/jssc

Synthesis, structure and electric studies for $La_{0.7}A_{0.3}Mn_{0.96}(In_xAl_{(1-x)})_{0.04}O_3$; A = Ca and Sr perovskites

M.F. Mostafa[a], S.S. Ata-Allah[b], H.S. Refai[b,*]

[a]*Physics Department, Faculty of Science, University of Cairo, Gaza, Egypt*
[b]*Reactor and Neutron Physics Department, Nuclear Research Center, Atomic Energy Authority, Cairo, Egypt*

Received 21 November 2007; received in revised form 21 January 2008; accepted 22 January 2008
Available online 7 February 2008

Abstract

Two polycrystalline series of samples in the form $La_{0.7}A_{0.3}Mn_{0.96}(In_xAl_{(1-x)})_{0.04}O_3$; A = Ca and Sr with ($0.0 \leqslant x \leqslant 1.0$) were synthesized using solid-state reaction. Rietveld analysis of the X-ray powder diffraction showed that, the Ca-series has an orthorhombic unit cell (space group *Pnma*) and the Sr-series is rhombohedral with (space group $R\bar{3}C$). Structural parameters (refined lattice parameters, atom positions, bond distance, bond angles, valence sum, valence bond, bond lengths and bond angles) are reported and discussed as a function of In content for the two series. Resistivity measurements in zero field are carried out in the range 50–300 K for the Ca-series and in the range 300–400 K for the Sr-series. The obtained transition temperature T_ρ at which the metal-semiconducting (MS) occurred, is discussed as a function of the compositional parameter x.

Keywords: Perovskite; Structure parameters; Bond valance; Bond angles; Bond distance; SEM; Metal–semiconductor transition

1. Introduction

Perovskite oxides, ABO_3, have been extensively studied due to their unique and applicable properties. The B-site ions coordinate with six oxygen ions and the octahedra share corners along the crystallographic x-, y-, and z-axis in ABO_3 [1–5]. The superexchange interactions between magnetic B-ions through oxygen ions have an effect on magnetic and electrical properties. The electrical properties can be partially improved by substitution of a metal with different valence state and ionic radius in the A- and B-sites. Much effort has been devoted to these materials, since the discovery of the colossal magnetoresistance (CMR) effect in manganese oxides referred to as manganites. In an attempt to relate the structure to the electronic and magnetic properties, Hwang et al. [6] and Damay et al. [7] proposed phase diagrams for $R_{1-x}A_xMnO_3$. They classified the manganites according to their tolerance factor ($t = (d_{A-O})/\sqrt{2}(d_{Mn-O})$). This provides a clue for tracing the diverse behavior of these materials, where for $t<1$, usually smaller Mn–O–Mn bond angles result and consequence of the rotation and deformation of the MnO_6 octahedra occurred. This leads to the weakness of the double-exchange (DE) coupling between Mn^{3+} and Mn^{4+} ions and causing a decrease in Curie temperature. Radealli et al. [8] and Millis et al. [9,10] found that, the lattice polaron (e.g. Jahn–Teller polaron) may couple to the structure details beyond the capture of a tolerance factor. This may play an important role in determining the properties of $R_{1-x}A_xMnO_3$, together with studies on the effect of cation disorder [11,12].

In fact, the size mismatch between A and B cations in the ABO_3 type perovskite can be controlled not only by changing the size of A but also the size of B. It is well known that, most of these compounds show a relation between small structure changes and their physical properties [13]. The understanding of these properties needs an accurate structural determination. The present work is devoted to the synthesis of $La_{0.7}A_{0.3}Mn_{0.96}(In_xAl_{(1-x)})_{0.04}$

*Corresponding author.
E-mail address: hananrefai@yahoo.com (H.S. Refai).

0022-4596/$ - see front matter © 2008 Elsevier Inc. All rights reserved.
doi:10.1016/j.jssc.2008.01.038

O_3; $A = Ca$ and Sr perovskites with x ranges from 0.0 to 1.0 in order to determine the structural parameters and investigate their electric properties.

2. Experimental details

Perovskite-type compounds with nominal stoichiometry $La_{0.7}A_{0.3}Mn_{0.96}(In_xAl_{(1-x)})_{0.04}O_3$; $A = Ca$ and Sr with $(0.0 \leqslant x \leqslant 1.0)$ were synthesized by conventional solid-state reaction with starting materials of spectroscopically pure La_2O_3, CaO, SrO, Mn_2O_3, Al_2O_3, and In_2O_3. The starting materials corresponding to each composition were intimately mixed in agate mortar. Samples were heated in air for 30 h at 1000 °C (Sr-series) and 1100 °C (Ca-series). The products were reground, pressed into pellets and fired again for the same duration at 1100 °C (Sr-series) and 1200 °C (Ca-series). This process was repeated at the same conditions to ensure a complete reaction. The obtained products were reground, pressed into the desired shapes then sintered in air for 96 h at 1180 °C (Sr-series) and 1280 °C (Ca-series) with intermediate grinding and pressing.

X-ray diffraction (XRD) patterns were obtained at room temperature using the Semiens-D5000 diffractometer with Cu$K\alpha$ radiation in the angle range $(10° < 2\theta < 90°)$ with 0.02° steps. The instrumental resolution was 0.004–0.005° over this 2θ range. XRD data were analyzed with the use of Rietveld method [14]. Bond valence analyses were performed using a PC version program package [15].

Resistivity measurements were carried out on cooling and heating modes in the range 50–300 K for the Ca-series $La_{0.7}Ca_{0.3}Mn_{0.96}(In_xAl_{(1-x)})_{0.04}O_3$ using a computerized four-probe technique with closed cycle refrigerator from Janis Research Co. Inc. Models CCS-3505. Whereas, the Sr-series $La_{0.7}Sr_{0.3}Mn_{0.96}(In_xAl_{(1-x)})_{0.04}O_3$ was measured in the range 300–400 K using a modified cryostat from Janis Research Co. Inc. Model DCD-300 with a computerized conventional four-probe technique. Measurements for the two series of samples were carried out on a regular bar on which four electrical leads are regularly arranged with silver paste epoxy using Keithley 224 programmable current source and Keithley 182 sensitive digital voltmeter. The current is adjusted to maintain I–V characteristic within the linear range. The temperature was controlled using Lakeshore 330 auto tuning temperature controller. Data logger software was designed using Lab View for controlling and collecting the data through IEEE-488 GPIB interfaces with the different equipments.

3. Results and discussion

3.1. Phase analysis

The nominal and analytical compositions of the prepared compounds in the present research work were examined using energy-dispersive X-ray (EDX) technique, where the determined results are given in Table 1. These results are compared with the nominal compositions used

Table 1
The elemental analysis obtained from (EDX) analysis and the theoretical calculations for the perovskite series $La_{0.7}\square_\delta Ca_{0.3+\delta}Mn_{0.96}In_{0.04x}Al_{(1-x)0.04}O_3$ and $La_{0.7}\square_\delta Sr_{0.3-\delta}Mn_{0.96}In_{0.04x}Al_{(1-x)0.04}O_3$

Sample x	Mol. weight	La		Ca		Mn		Al		In	
		Calc.	Exp.	Calc.	Exp.	Calc.	Exp.	Calc.	Exp.	Calc.	Exp.
0.0	211.0758	46.0658	51.71±0.15	5.6965	5.47±0.04	24.9865	27.70±0.12	0.5113	0.42±0.03	0	0
0.2	211.7785	45.9130	46.95±0.12	5.6965	10.38±0.05	24.9036	26.24±0.10	0.4077	0.38±0.02	0.43374	0.34±0.07
0.4	212.4812	45.7612	46.99±0.16	5.6589	10.39±0.06	24.8212	25.90±0.13	0.3048	0.30±0.03	0.86460	0.65±0.08
0.6	213.1839	45.6103	46.95±0.14	5.6402	10.9±0.06	24.7394	25.47±0.11	0.2025	0.20±0.02	1.2926	1.05±0.08
0.8	213.8866	45.4605	46.56±0.16	5.6217	10.27±0.06	24.6581	25.26±0.13	0.1009	0.13±0.03	1.71785	1.46±0.09
1.0	214.5893	45.3116	47.87±0.15	5.6033	9.71±0.06	24.5774	25.44±0.12	0	0	2.14027	1.91±0.09
Sample x	Mol. weight	La		Sr		Mn		Al		In	
		Calc.	Exp.	Calc.	Exp.	Calc.	Exp.	Calc.	Exp.	Calc.	Exp.
0.2	226.0405	43.0161	50.22±0.23	11.6289	6.93±0.09	23.3323	27.49±0.16	0.3820	0.31±0.03	0.4064	0.30±0.09
0.4	226.7432	42.8828	49.85±0.23	11.5929	6.95±0.09	23.26	26.85±0.16	0.2855	0.23±0.03	0.8102	0.87±0.09
0.6	227.4459	42.7503	49.58±0.23	11.5570	8.03±0.11	23.1881	25.35±0.16	0.1898	0.21±0.03	1.2116	1.14±0.10
0.8	228.1486	42.6186	51.55±0.17	11.5214	7.04±0.09	23.1167	27.08±0.15	0.0946	0.13±0.03	1.6105	1.45±0.10
1.0	228.8513	42.4878	52.41±0.17	11.4861	6.82±0.09	23.0457	26.76±0.14	0	0	2.0069	1.80±0.10

in the preparation of the raw materials. No significant differences between analytical and nominal compositions for $La_{0.7}Ca_{0.3}Mn_{0.96}In_{0.04x}Al_{(1-x)0.04}O_3$ (Ca-series) and $La_{0.7}Sr_{0.3}Mn_{0.96}In_{0.04x}Al_{(1-x)0.04}O_3$ were observed. However, in the range $0.2 \leqslant x \leqslant 1.0$ the data show that, values of Ca_{calc} are less than Ca_{exp} and values of Sr_{calc} are greater than Sr_{exp} as given in Table 1. This could be attributed to the fact that there is a vacancy with average radius $\langle r_A \rangle \neq 0$. This radius $\langle r_A \rangle$ could be greater than that of Ca^{2+} or Sr^{2+} ions and less than that of La^{3+} ion. Replacing Al^{3+} (0.535 Å) [16] with In^{2+} (0.8 Å) [16] at the *B*-site in the perovskite unit cell will enhance the MO_6 octahedron by producing a long average *M*–O distance. In this regard, the differences between the analytical (calc.) and nominal (exp.) values of Ca and Sr permits the use of the nominal composition of the two perovskite series as: $La_{0.7}\square_{\delta}Ca_{0.3+\delta}Mn_{0.96}In_{0.04x}Al_{(1-x)0.04}O_3$ (Ca-series) and $La_{0.7}\square_{\delta}Sr_{0.3-\delta}Mn_{0.96}In_{0.04x}Al_{(1-x)0.04}O_3$ (Sr-series).

3.2. Crystal structure

Results of indexing the XRD patterns of the prepared samples indicate that the nominal compositions with different concentrations are single-phase with no additional lines corresponding to any other phases. The full-width at half-maximum (FWHM) was found to be ~0.05° indicating good crystallinity and homogeneity for the prepared samples.

3.2.1. Al- and In-doped La–Ca manganite $La_{0.7}\square_{\delta}Ca_{0.3+\delta}Mn_{0.96}In_{0.04x}Al_{(1-x)0.04}O_3$

Fig. 1 illustrates the XRD patterns of the (Al and In)-doped La–Ca manganite at room temperature, where the peaks are quite sharp for the indexing process. The analysis of the full XRD patterns of the individual reflections of these samples (Fig. 1) indicate that they are crystallized in orthorhombic unit cell. The systematically absent reflections are consistent with the space group *Pnma*. The X-ray diagrams obtained for this series are quite similar to that of $LaMnO_3$ except for the difference in line splitting, where the degree of line splitting decreased with calcium substituted La in $LaMnO_3$ sample [17,18]. The XRD patterns clearly shows that there is no appreciable difference in the positions of the various peaks among the various doped samples compared with that of the $La_{0.7}Ca_{0.3}MnO_3$.

In the RMO_3 perovskite with the orthorhombic structure, rare-earth cations (*R*) are placed in 4*c* sites $\pm(x, y, \frac{1}{4}; \frac{1}{2}-x, \frac{1}{2}+y, \frac{1}{4})$, the transition metal cations (*M*) in 4*b* sites on the symmetry center $(\frac{1}{2}, 0, 0; \frac{1}{2}, 0, \frac{1}{2}; 0, \frac{1}{2}, 0; 0, \frac{1}{2}, \frac{1}{2})$. Oxygen ions, O (2), are in $8d \pm (x, y, z; \frac{1}{2}-x, \frac{1}{2}+y, \frac{1}{2}-z; -x, -y, \frac{1}{2}+z; \frac{1}{2}+x, \frac{1}{2}-y, -z)$ and the apical oxygen ions, O (1), are in 4*c* sites. Lattice parameters, fractional atomic coordinates were obtained from the Rietveld analysis [14]. A pseudo-Voigt function is selected as the diffraction peak shape function. Background coefficients, zero point, a scale factor, an asymmetry parameter for the shape of the peak and profile shape parameters are also refined in the final run.

The lattice parameters and the unit cell volume of this series are given in Table 2 where the data show that: first, the unit cell volume of the undoped sample ($La_{0.7}Ca_{0.3}MnO_3$) is decreased compared with $LaMnO_3$ sample [17,18]. This contraction of the unit cell is attributed to the increase of Mn^{4+} content [19], where the ionic radius of Mn^{4+} [with coordination VI] (0.53 Å) in an octahedral *B*-site is smaller than that of Mn^{3+} [with coordination VI] (0.645 Å) [16].

Second, as the compositional parameter *x* increases the lattice parameters increase as a general trend. This could be attributed to the ionic radii of In^{3+} [with coordination VI] (0.8 Å) which is larger than that of Al^{3+} [with coordination VI] (0.535 Å) [16].

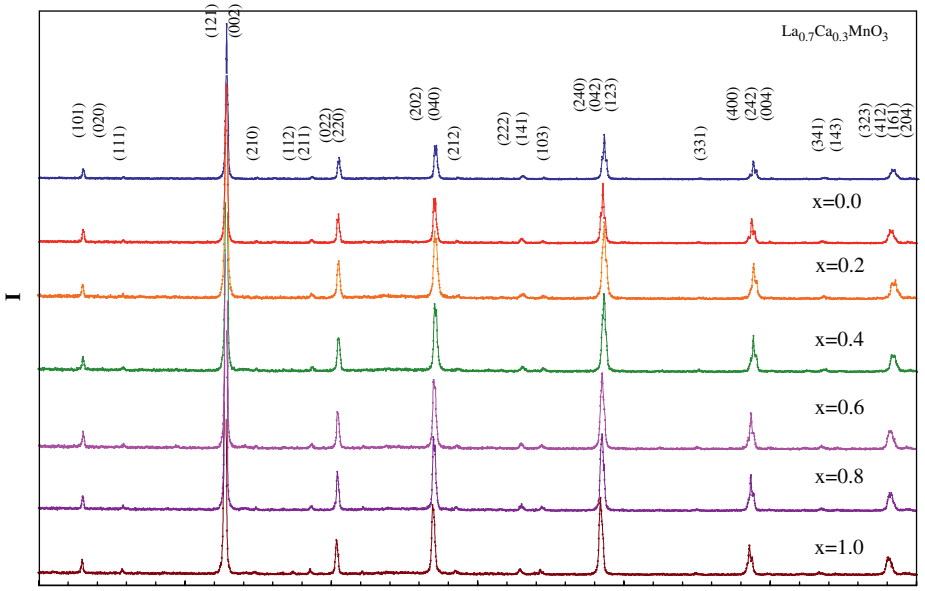

Fig. 1. XRD patterns of $La_{0.7}Ca_{0.3}MnO_3$ and $La_{0.7}Ca_{0.3}Mn_{0.96}(In_xAl_{(1-x)})_{0.04}O_3$.

Table 2
Refined lattice parameters in Å and tolerance factor (t) with the reliability (weighted R_{wp} and unweighted R_p) factors for $La_{0.7}Ca_{0.3}MnO_3$, and $La_{0.7}\square_\delta Ca_{0.3+\delta}Mn_{0.96}(In_xAl_{(1-x)})_{0.04}O_3$

Sample	R_{wp}	R_p	a (Å)	b (Å)	c (Å)	V (Å^3)	t
$La_{0.7}Ca_{0.3}MnO_3$	10.43	7.46	5.6154(2)	7.8067(3)	5.4349(1)	238.2538	0.9357
$x = 0.0$	11.22	8.25	5.5684(3)	7.7656(4)	5.4205(1)	234.3931	0.9556
$x = 0.2$	10.18	7.21	5.6154(2)	7.7676(4)	5.4208(1)	236.4454	0.9550
$x = 0.4$	9.92	6.95	5.5775(1)	7.7739(2)	5.4237(3)	235.1658	0.9536
$x = 0.6$	9.85	6.88	5.5838(2)	7.7800(1)	5.4264(3)	235.7335	0.9523
$x = 0.8$	9.75	6.78	5.5901(1)	7.7862(3)	5.4292(2)	236.3094	0.9509
$x = 1.0$	10.50	7.53	5.5936(1)	7.7903(2)	5.4316(2)	236.6864	0.9503

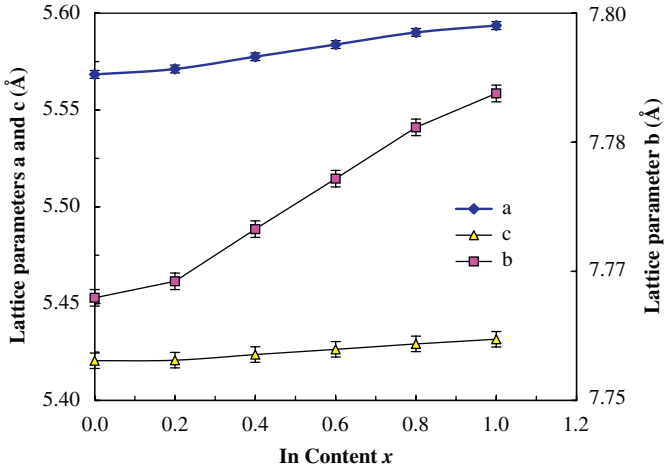

Fig. 2. Lattice parameters versus In content x for the perovskite series $La_{0.7}Ca_{0.3}Mn_{0.96}(In_xAl_{(1-x)})_{0.04}O_3$.

It is well known that, homogeneous and random solid solutions usually obey the so-called Vegard's law, i.e. a linear dependence between composition and structural parameters [20]. In the presently studied samples (Fig. 2) the Vegard's law is obeyed in the range $0.2 \leqslant x \leqslant 1.0$. There are nonlinear modulations due to the nonlinear dependence of the structural parameter at $x \leqslant 0.2$. This likely suggests that the structure variations are not due to steric effect only but some electronic factors must also be considered in the M sublattice.

The refined atomic position obtained from the XRD analysis is given in Table 3. The results are consistent within the standard deviations. The calculated structure parameters for the present series of perovskite samples given in Table 3 indicate that, the doped lanthanum calcium manganites have solid solutions with replacement of Al and In for Mn and exhibit full occupancies in the metal sublattices, i.e. the (La + Ca) and (Mn + Al + In) occupancies both equal unity.

The bond lengths and angles are calculated using the coordinates from the Rietveld analysis. The Mn–O distances calculated from the refined structure are given in Table 4. The Mn–O (1 and 2) distances is found to be decreased for $La_{0.7}Ca_{0.3}MnO_3$ compared with $LaMnO_3$ sample [17,18] due to the increase of Mn^{4+} amount as Ca^{2+} replaces La^{3+} in this compound [19]. The data shows that the bond distances are decreased as Al substitutes for Mn (sample with $x = 0.0$) then increased with increasing *In* content x. However, the bond angles are increased with substituting Al at $x = 0.0$ then decreased as In content increases as clearly shown in Tables 5 and 6.

In perovskite materials, there are two important structural effects: firstly, the distortion that occurs in the

Table 3
Refined atom positions for $La_{0.7}Ca_{0.3}MnO_3$, and the perovskite series $La_{0.7}\square_\delta Ca_{0.3+\delta}Mn_{0.96}(In_xAl_{(1-x)})_{0.04}O_3$

Sample	Atom	Position	x	y	z
$La_{0.7}Ca_{0.3}MnO_3$	La, Ca	4(c)	0.5524	0.2500	0.5177
	Mn	4(b)	0.5000	0.0000	0.0000
	O(1)	4(c)	−0.0158	0.2500	0.4081
	O(2)	8(d)	0.2930	0.0489	0.7041
$x = 0.0$	La, Ca	4(c)	0.5429	0.2500	0.5140
	Mn, Al	4(b)	0.5000	0.0000	0.0000
	O(1)	4(c)	−0.0131	0.2500	0.4168
	O(2)	8(d)	0.2894	0.0416	0.7084
$x = 0.2$	La, Ca	4(c)	0.543(7)	0.2500	0.5143
	Mn, Al, In	4(b)	0.5000	0.0000	0.0000
	O(1)	4(c)	−0.0133	0.2500	0.4161
	O(2)	8(d)	0.2897	0.0419	0.7081
$x = 0.4$	La, Ca	4(c)	0.5447	0.2500	0.5147
	Mn, Al, In	4(b)	0.5000	0.0000	0.0000
	O(1)	4(c)	−0.0136	0.2500	0.4152
	O(2)	8(d)	0.2901	0.0424	0.7076
$x = 0.6$	La, Ca	4(c)	0.5457	0.2500	0.5151
	Mn, Al, In	4(b)	0.5000	0.0000	0.0000
	O(1)	4(c)	−0.0139	0.2500	0.4142
	O(2)	8(d)	0.2905	0.0429	0.7071
$x = 0.8$	La, Ca	4(c)	0.5468	0.2500	0.5155
	Mn, Al, In	4(b)	0.5000	0.0000	0.0000
	O(1)	4(c)	−0.0142	0.2500	0.4133
	O(2)	8(d)	0.2909	0.0434	0.7066
$x = 1.0$	La, Ca	4(c)	0.5471	0.2500	0.5157
	Mn, In	4(b)	0.5000	0.0000	0.0000
	O(1)	4(c)	−0.0143	0.2500	0.4130
	O(2)	8(d)	0.2910	0.0435	0.7065

Table 4
Bond distances of $La_{0.7}Ca_{0.3}MnO_3$, and the perovskite series $La_{0.7}\square_{\delta}Ca_{0.3+\delta}Mn_{0.96}(In_xAl_{(1-x)})_{0.04}O_3$

Sample	Mn–O(1 and 2)	La–O(1)	La–O(2)	Ca–O(1)	Ca–O(2)
$La_{0.7}Ca_{0.3}MnO_3$	2.0165	2.8079(3)	2.7935(3)	2.8079(3)	2.7935(3)
$x=0.0$	1.9944	2.7814(5)	2.7711(5)	2.7814(5)	2.7711(5)
$x=0.2$	1.9958	2.7829(5)	2.7723(8)	2.7829(5)	2.7723(8)
$x=0.4$	1.9986	2.7864(5)	2.7755(3)	2.7864(5)	2.7755(3)
$x=0.6$	2.0014	2.7897(2)	2.7783(8)	2.7897(2)	2.7783(8)
$x=0.8$	2.0042	2.7933(3)	2.7964(5)	2.7933(3)	2.7964(5)
$x=1.0$	2.0057	2.7953(3)	2.7832(8)	2.7953(3)	2.7832(8)

Table 5
Mn–O–Mn angles for $La_{0.7}Ca_{0.3}MnO_3$, and the perovskite series $La_{0.7}\square_{\delta}Ca_{0.3+\delta}Mn_{0.96}(In_xAl_{(1-x)})_{0.04}O_3$

Sample	Mn–O(1)–Mn	Mn–O(2)–Mn
$La_{0.7}Ca_{0.3}MnO_3$	150.87	151.33
$x=0.0$	153.53	153.87
$x=0.2$	153.31	153.67
$x=0.4$	153.03	153.39
$x=0.6$	152.72	153.10
$x=0.8$	152.44	152.83
$x=1.0$	152.35	152.75

structure as a result of the size mismatch between Mn (B-site cations) on one hand, and the R^{3+} (rare-earth element) and A^{2+} (e.g. Ca or Sr) at A-site on the other hand. This distortion in $RMnO_3$ perovskite structure is measured using a tolerance factor (t), where

$$t=\frac{(R-O)}{\sqrt{2}(M-O)}.$$

In this case, the measure of the mismatch between the equilibrium R–O and M–O bond length is the deviation of (t) from unity, where $t\cong 1.0$ allows stabilization of intergrowth structures.

The value of t may be calculated from the sums of empirical ionic radii of the perovskite ABO_3 as

$$t=\frac{(r_A+r_O)}{\sqrt{2}(r_B-r_O)}.$$

For most of the CMR manganese perovskite $t<1$, which implies that the cage formed by corner sharing MnO_6 octahedra is too large for cations at the A-sites, and the structure is distorted by twisting and tilting the MnO_6 octahedra. Such a distortion results in a bending of Mn–O–Mn bond, a weakening of the DE interaction and a reduction of the width of the conduction bond [21,22]. Values of the tolerance factor (t) for the present series are given in Table 2, where they are in good agreements with most reported values for Ca-doped $LaMnO_3$ [19].

The second structural effect is the size and charge difference between the R^{3+} and (Ca^{2+} or Sr^{2+}) cations which are being randomly distributed over the A-sites. This will cause inhomogeneity in the background potential experienced by e_g electrons as they move through the crystal, leading to some regions of low potential in which the electrons can be trapped. There are two mechanisms to achieving this:

- The first mechanism is the direct interactions of the electrons with charges and relaxed environments around the static arrangement of R^{3+} and (Ca^{2+} or Sr^{2+}) cations. This will tend to localize the electrons close to the R^{3+} ions.
- The second mechanism is the dynamic electron–phonon coupling between the Mn^{3+}–O and Mn^{4+}–O bonds, a difference which provides a coupling between the electron and the octahedral breathing-mode phonon. This mechanism arises from Jahn–Teller distortion that occurs around the Mn^{3+}, but not around Mn^{4+}, which provides a coupling between the electron and a tetragonal distortion mode of the MnO_6 octahedra.

On the other hand, bond valence calculations are performed for the present studied materials. In this concern, the bond valence model [23] describes a phenomenological correlation between the formal valence of a bond and the bond lengths around it. The bond valence, S_{ij}, associated with each cation–anion interaction is calculated using

$$S_{ij}=e^{(R_{ij}-d_{ij})/B},$$

where d_{ij} is the cation–anion distance and B is an empirically determined parameter, but can often be treated as a universal constant with a value of 0.37. R_{ij} is empirically determined for each cation–anion pair based upon a large number of well-determined bond distances for the cation–anion pair in question.

R_{ij} constants are calculated from the equation [24]:

$$R_{ij}=B\ln\left[\frac{V_i}{\sum_j \exp\left(\frac{-d_{ij}}{B}\right)}\right].$$

The atomic valences, V_i(calc), of R and M cations and X anion in AMX_3 orthorhombic perovskite structures are calculated by summing the individual bond valences (S_{ij})

Table 6
Bond valences of $La_{0.7}Ca_{0.3}MnO_3$, and the perovskite series $La_{0.7}\square_{\delta}Ca_{0.3+\delta}Mn_{0.96}(In_xAl_{(1-x)})_{0.04}O_3$

Sample	Mn–O(1 and 2)	Al–O(1 and 2)	In–O(1 and 2)	La–O(1)	La–O(2)	Ca–O(1)	Ca–O(2)
$La_{0.7}Ca_{0.3}MnO_3$	0.5000	–	–	0.2919(7)	0.2845(5)	0.1678(0)	0.1653(2)
$x=0.0$	0.5274	0.3599	–	0.2861(3)	0.2815(8)	0.1644(0)	0.1618(0)
$x=0.2$	0.5254	0.3585	0.7741	0.2869(5)	0.2821(5)	0.1648(7)	0.1621(2)
$x=0.4$	0.5215	0.3557	0.7682	0.2873(3)	0.2818(3)	0.1651(2)	0.1619(5)
$x=0.6$	0.5173	0.3530	0.7623	0.2874(3)	0.2819(0)	0.1651(7)	0.1620(0)
$x=0.8$	0.5134	0.3503	0.7564	0.2874(3)	0.2818(5)	0.1651(8)	0.1619(7)
$x=1.0$	0.5110	–	0.7535	0.2869(0)	0.2812(7)	0.1648(7)	0.1616(2)

Table 7
Bond valences sum and Global instability factor of $La_{0.7}Ca_{0.3}MnO_3$, and the perovskite series $La_{0.7}\square_{\delta}Ca_{0.3+\delta}Mn_{0.96}(In_xAl_{(1-x)})_{0.04}O_3$

Sample	$La_{0.7}Ca_{0.3}MnO_3$	$x=0.0$	$x=0.2$	$x=0.4$	$x=0.6$	$x=0.8$	$x=1.0$
La	3.4444	3.3970	3.4049	3.4039	3.4051	3.4047	3.3978
Ca	1.9792	1.9520	1.9565	1.9560	1.9566	1.9564	1.9524
Mn	3.0000	3.1642	3.1522	3.1280	3.1040	3.0802	3.0682
Al	–	2.1591	2.1509	4.6092	2.1180	4.5387	–
In	–	–	4.6448	2.1344	4.5738	2.1018	4.5211
O(1)	1.4598	1.5341	1.5240	1.5247	1.5248	1.5247	1.5348
O(2)	1.4481	1.5269	1.5165	1.5160	1.5161	1.5159)	1.5259
GII	0.0979	0.4240	0.4054	0.4085	0.4112	0.4135	0.4333

about each ion

$$V_{i(\mathrm{calc})} = \sum_j S_{ij}.$$

Six nearest neighbor anions are used for the M cation, six nearest neighbor cations for the anion (O) and 12 nearest neighbor anions for the R-site cation are used in the calculations. No assumption is made about the coordination number of the A-site cation. The B cations remain at fixed positions in all space groups generated by simple tilting of the MO_6 octahedra. M–O bond distance, which determines the size of the octahedron, is calculated so as to optimize the bond valence sum of the octahedral cation. O–M–O bond angles of the MO_6 octahedra remain ideal (90°) and M–O bond distances are held constant in the calculations. Valence sum of A-site cation is varied by changing the size of octahedral tilting distortion. The optimized structure is done by minimizing the difference between calculated bond valence sum and formal valence of each ion. This value is termed, the discrepancy factor d [25], which measures the lattice strains present in the compound and is calculated according to:

$$d_i = V_{i(\mathrm{ox})} - V_{i(\mathrm{calc})},$$

where V_i(ox) is the formal valence and V_i(calc) is the calculated bond valence sum for the ith ion. The overall structure stability is determined by comparing the calculated bond valence sums with the ideal formal valences. This quantity is referred to as the global instability index (GII) and is calculated according to [26]

$$\mathrm{GII} = \sqrt{\frac{\sum_{i-1}^{N}(d_1^2)}{N}}.$$

Variables involved in GII equation are discrepancy factor (d_i) and N, which is the number of atoms in the formula unit. During the optimization process the octahedral tilt angle is stepped incrementally and the individual A–O and M–O bond distances, discrepancy factors and GII are calculated at each step.

The GII value is typically <0.1 valence units (v.u.) for unstrained structures. In a structure with lattice-induced strains the Global instability GII is (>0.1 v.u.). Table 7 lists the calculated valence sum of the present studied Ca-series associated with the GII. The data given in this table clearly show unstrained structure where, the value of GII is 0.097 v.u. for $La_{0.7}Ca_{0.3}MnO_3$.

The values of bond valence sum show insignificant dependence on the compositional parameter x as given in Table 7. For the present Ca-series the values of the Global instability factor (Table 7) show clear evidence for lattice with induced strain (GII >0.1).

3.2.2. La–Sr-doped Al and In manganites $La_{0.7}\square_{\delta}Sr_{0.3-\delta}Mn_{0.96}In_{0.04x}Al_{(1-x)0.04}O_3$

Fig. 3 illustrates the X-ray powder diffraction patterns of $La_{0.7}Sr_{0.3}MnO_3$ and the series $La_{0.7}\square_{\delta}Sr_{0.3-\delta}Mn_{0.96}In_{0.04x}Al_{(1-x)0.04}O_3$ ($0.0\leqslant x\leqslant 1.0$) with step of 0.2. The figure shows that all the studied samples have a single-phase

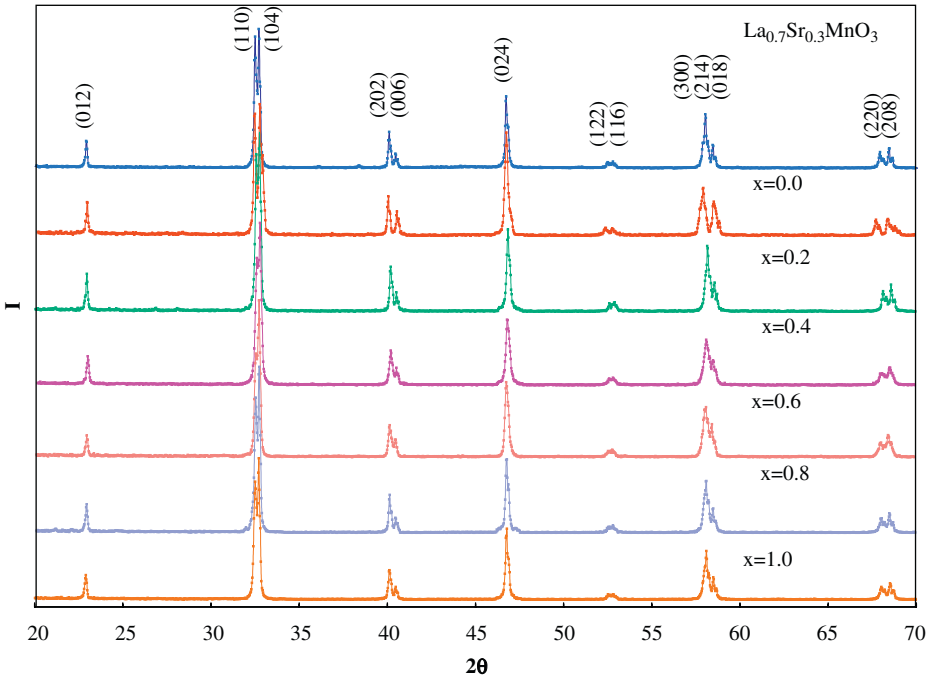

Fig. 3. XRD patterns of $La_{0.7}Sr_{0.3}MnO_3$ and $La_{0.7}Sr_{0.3}Mn_{0.96}(In_xAl_{(1-x)})_{0.04}O_3$.

Table 8
Refined lattice parameters in Å and tolerance factor (t) with the reliability (weighted R_{wp} and unweighted R_p) factors for $La_{0.7}Sr_{0.3}MnO_3$, and the perovskite series $La_{0.7}\square_\delta Sr_{0.3-\delta}Mn_{0.96}(In_xAl_{(1-x)})_{0.04}O_3$

Sample	R_{wp}	R_p	a (Å)	c (Å)	V (Å^3)	T
$La_{0.7}Sr_{0.3}MnO_3$	10.43	7.46	5.5461	13.9705	372.15	0.9516
$x = 0.0$	11.22	8.25	5.5227	13.9317	367.99	0.9698
$x = 0.2$	10.18	7.21	5.5049	13.8272	362.88	0.9712
$x = 0.4$	9.92	6.95	5.5080	13.8467	363.81	0.9698
$x = 0.6$	9.85	6.88	5.5111	13.8663	364.72	0.9685
$x = 0.8$	9.75	6.78	5.5143	13.8858	365.66	0.9671
$x = 1.0$	10.50	7.53	5.5358	14.0098	371.81	0.9489

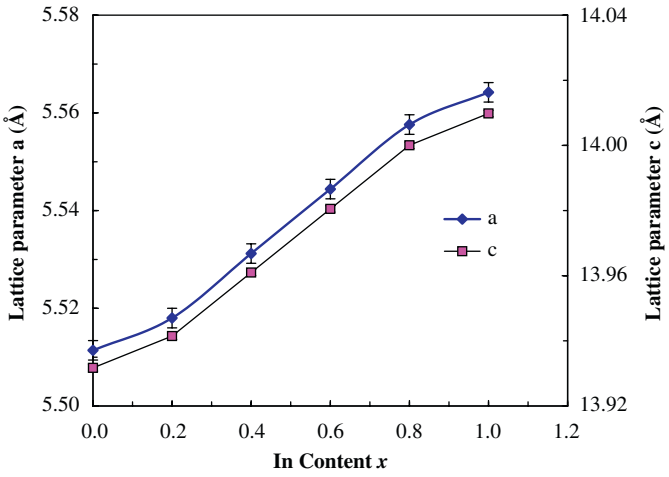

Fig. 4. Lattice parameters versus In content x for the perovskite series $La_{0.7}Sr_{0.3}Mn_{0.96}(In_xAl_{(1-x)})_{0.04}O_3$.

Table 9
Refined atom positions for $La_{0.7}Sr_{0.3}MnO_3$, and the perovskite series $La_{0.7}\square_\delta Sr_{0.3-\delta}Mn_{0.96}(In_xAl_{(1-x)})_{0.04}O_3$

Sample	Atom	Position	x	y	z
$La_{0.7}Sr_{0.3}MnO_3$	Mn	(6*b*)	0.6667	0.3333	0.3333
	O	(18*e*)	0.5693	0.0000	0.2500
$x = 0.0$	Mn, Al	(6*b*)	0.6667	0.3333	0.3333
	O	(18*e*)	0.4289	0.0000	0.2500
$x = 0.2$	Mn, Al, In	(6*b*)	0.6667	0.3333	0.3333
	O	(18*e*)	0.5655	0.0000	0.2500
$x = 0.4$	Mn, Al, In	(6*b*)	0.6667	0.3333	0.3333
	O	(18*e*)	0.4334	0.0000	0.2500
$x = 0.6$	Mn, Al, In	(6*b*)	0.6667	0.3333	0.3333
	O	(18*e*)	0.5678	0.0000	0.2500
$x = 0.8$	Mn, Al, In	(6*b*)	0.6667	0.3333	0.3333
	O	(18*e*)	0.5688	0.0000	0.2500
$x = 1.0$	Mn, In	(6*b*)	0.6667	0.6667	0.3333
	O	(18*e*)	0.5687	0.5750	0.2500

rhombohedral-like perovskite structure with the $R\bar{3}C$ space group. There is no appreciable difference in the diffraction patterns or positions of the various peaks among the various In-doped samples compared with that of the $La_{0.7}Sr_{0.3}MnO_3$. Also, the peaks are sharp quite enough for the indexing. The lattice parameters and cell volume of Sr-series are given in Table 8. It is obvious that, the cell parameters of this series decreases as Al (0.535 Å) substitutes for Mn [Mn^{4+} (0.53 Å) and Mn^{3+} (0.645 Å)]. As In (0.8 Å) replaces Al in this series the cell parameters

increases as displayed in Fig. 4. The values of tolerance factor (t) given in Table 8 for this series are in good agreement with reported values for Sr-doped $LaMnO_3$ [19].

It was initially supposed that, the occupancies of oxygen and metal ions equal to the ideal values. The amplitude of dispersion of X-rays by oxygen is small and therefore the oxygen nonstoichiometry was set to remain at the ideal value of 3. Debye–Waller factor was taken equal to zero, and the occupancies of the cations (lanthanum, strontium and the 3*d*-metals (Mn)) were refined. The results of the refinement are given in Table 9. They indicate that Sr-doped lanthanum manganite has formed solid solution with the replacement of La by Sr.

The determined structure parameters of the present Sr-series given in Table 9, indicate that Sr-doped lanthanum manganites have solid solutions with a replacement of Al and In for Mn in this unit cell. This means a full occupancies in the metal sublattices, i.e. the (La + Sr) and (Mn + Al + In) occupancies both equal unity.

The values obtained for bond distances, bond angles, bond valence and valence sum (Table 10) of this series have decreased with the substitution of Al in place of Mn in $La_{0.7}Sr_{0.3}MnO_3$. But as In is introduced $La_{0.7}\square_{\delta}Sr_{0.3-\delta}Mn_{0.96}Al_{0.04}O_3$ in place of Al these values increases. This may be due to the decreasing amount of Mn^{4+} by increasing In content. The values obtained for the Global instability factor of these samples (Table 10) show unstrained structure GII (~0.2 v.u.).

In most studies, the grain sizes are estimated using XRD coupled with direct measurement of grain sizes using transmission electron microscope (TEM) [27–31]. Although the grain sizes are estimated from XRD can be independently corroborated via TEM, the determination of the grain size often relies on XRD only [27,28,30–32]. One of the most often used approaches in estimating the grain size from the XRD data is the utilization of Scherrer formula [33] which has the following form:

$$W_f = \frac{0.9\lambda}{D\cos\theta_D},$$

where W_f is the width at half-maximum intensity of Bragg reflection excluding instrumental broadening, λ the wavelength of the X-ray radiation, D the average crystallite size, and θ_D the Bragg angle. The X-ray line broadening method is used for the size determination of small crystallites (~100 nm). SEM micrographs showed that the microstructure of the present samples is homogeneous with particle size comparable with this range as seen in Fig. 5. The calculated values of the grain size for the present (Ca- and Sr-series) diluted with (Al and In) are given in Table 11. The values reveal that the grain size increases with increasing In concentration, where minimum grain size of about 79.5 nm corresponding to $x = 0.2$ is obtained for Ca-series. Although the crystal symmetry of these samples remains the same, the lattice parameters of Ca-series change slightly systematically with the grain size. These changes in lattice parameters may result from the increase in oxygen content, which increase the concentration of holes in the system and leads to a decrease in the structural distortion. In contrast with these results, the values of the grain size of the Sr-series have no significant changes with In content as given in Table 11. More homogeneity with smaller grain size is clearly observed from SEM micrograph in Fig. 5b for this series.

3.3. Electrical resistivity

Fig. 6 illustrates the variation of normalized resistivity with temperature of the Ca-series at zero magnetic field in the temperature range (50–300 K). The relation shows semiconducting behavior at high temperature. As temperature decreased, ρ increases reaching a maximum where

Table 10
Bond distances, bond angles, bond valence, bond valence sum and Global instability factor of $La_{0.7}Sr_{0.3}MnO_3$, and the perovskite series $La_{0.7}\square_{\delta}Sr_{0.3-\delta}Mn_{0.96}(In_xAl_{(1-x)})_{0.04}O_3$

Sample	$La_{0.7}Sr_{0.3}MnO_3$	$x = 0.0$	$x = 0.2$	$x = 0.4$	$x = 0.6$	$x = 0.8$	$x = 1.0$
Bond distance							
M(6*b*)–O(18*e*) × 2	2.0165	2.0109	1.9958	1.9986	2.0014	2.0042	2.0221
Bond angles							
Mn(4*b*)–O(18*e*)–Mn(4*b*)	166.88	166.58	167.52	167.35	167.13	166.95	165.90
Bond valence							
Mn(6*b*)–O(18*e*) × 2	0.5000	0.5076	0.5353	0.5213	0.5173	0.5134	0.4924
Al (6*b*)–O(18*e*) × 2	–	0.3477	0.3585	0.3557	0.3530	0.3503	–
In (6*b*)–O(18*e*) × 2	–	–	4.6541	4.6513	4.9458	4.9512	4.9800
Bond valence sum							
Mn(6*b*)	3.0000	3.0457	3.1521	3.1280	3.1040	3.0802	2.9543
Al(6*b*)	–	2.0863	2.1509	2.1344	2.1180	2.1018	–
In(6*b*)	–	–	5.0260	5.0396	4.7193	4.7247	4.7549
O(18*e*)	1.8805	1.7718	1.7932	1.7881	1.7833	1.7782	1.7526
Global instability factor							
GII	0.1499	0.2344	0.2239	0.2213	0.2190	0.2171	0.2340

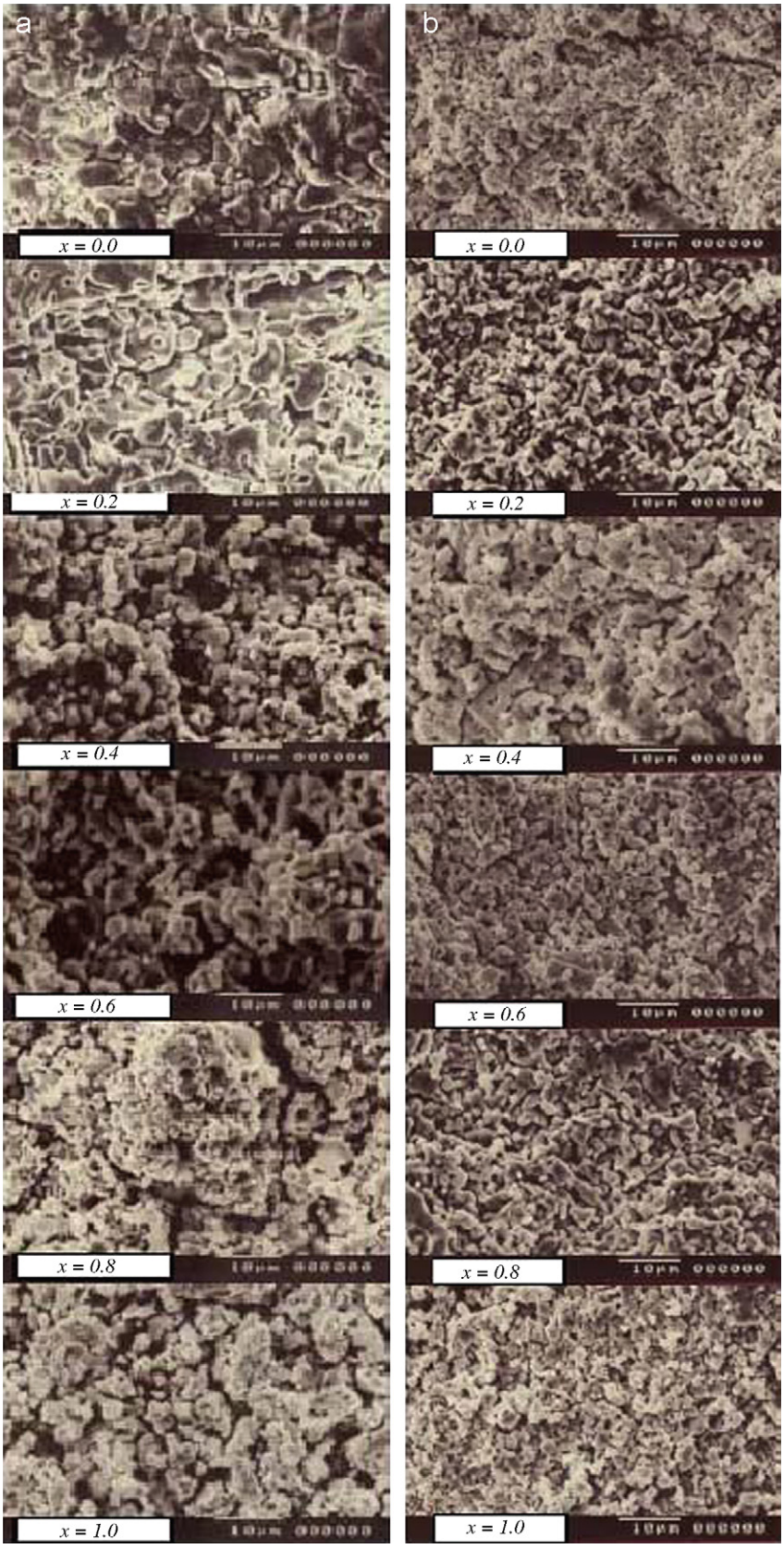

Fig. 5. SEM micrographs of (a) Ca-series and (b) Sr-series.

Table 11
Calculated values of the grain size for $La_{0.7}\square_{\delta}Ca_{0.3+\delta}Mn_{0.96}In_{0.04x}Al_{(1-x)0.04}O_3$ and $La_{0.7}\square_{\delta}Sr_{0.3-\delta}Mn_{0.96}In_{0.04x}Al_{(1-x)0.04}O_3$

Sample	D_{121} Ca-series	D_{104} Sr-series
$x=0.0$	102.3	41.3
$x=0.2$	79.5	41.3
$x=0.4$	82.6	40.9
$x=0.6$	94.2	44.7
$x=0.8$	95.4	42.1
$x=1.0$	102.2	39.7

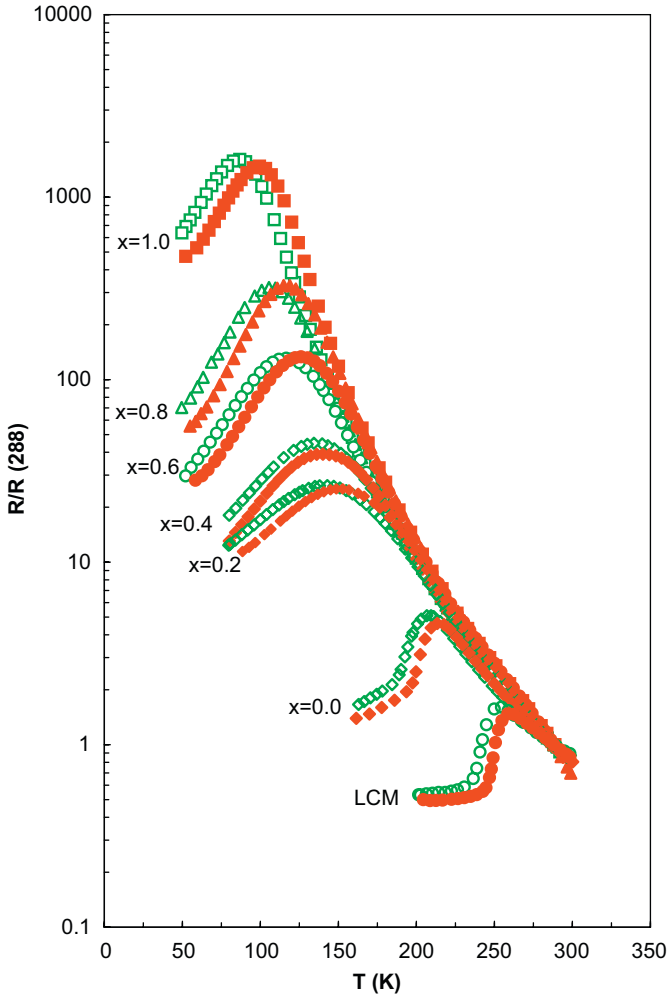

Fig. 6. Normalized $[R(T)/R(288\,K)]$ resistivity versus temperature for $La_{0.7}\square_{\delta}Ca_{0.3+\delta}Mn_{0.96}(In_xAl_{(1-x)})_{0.04}O_3$ perovskite system at zero magnetic field in the range (50–300 K). Open symbol for cooling and closed symbol for heating.

metallic behavior appears. The temperature, at which the semiconductor–metal (SM) transition T_ρ is occurred, is tentatively defined as the temperature at which the resistivity reaches its maximum value with temperature. In the present study, the determined T_ρ for the Ca-series decreases from $T_\rho = 219\,K$ at $x=0.0$ to $T_\rho = 96\,K$ at $x=1.0$. This corresponds to the values of ρ at these maxima ranging from 79 Ω cm to 76 kΩ cm as listed in Table 12.

The $\rho(T)$ curve measured upon heating and cooling for the present material as displayed in Fig. 6. The relation shows thermal hysteresis due to the fist-order character of the transition. At high temperature, $T>T_\rho$ the relation shows that, resistivity is almost insensitive to the In content. In contrast, at low temperature, $T<T_\rho$, a giant resistive peak develops and $\rho(T)$ relation exhibits a significant dependence on In content. At temperature well below the resistive peak, a metallic behavior is almost recovered. The most remarkable result is the monotonous increasing of T_ρ with In content. As shown in Fig. 7(a) and (b) the calculated amplitude of the zero-field resistivity peak is closely related to the In content and the transition temperature T_ρ.

Substitution of Al^{3+} with ionic radius (0.535 Å) in place of Mn^{3+} with ionic radius (0.645 Å) in the unit cell of $La_{0.7}Ca_{0.3}MnO_3$ decreases the resistive transition T_ρ in the present work with ($\Delta T_\rho = 50\,K$) this agrees with previous reports for Al doping of $La_{0.75}Ca_{0.35}MnO_3$ [34] and $La_{0.7}Ca_{0.3}MnO_3$ [35]. This suppression of T_ρ could be explained as follows: Al has no magnetic moment and no a DE interaction with Mn, it will decrease the metal–insulator transition temperature and signifies a weaker Al^{3+}–O–Mn^{4+} coupling. This emphasizes the strong correlation between the local magnetic polarization and transport in these materials. Thus, Al doping at Mn site affects the ferromagnetic coupling energy. This factor reflects that the Mn^{3+}–O–Mn^{4+} configuration prevailing in the region between the spin distortion regions near the Al sites are responsible for the observed transport features. As In substitutes Al in this perovskite system, a further decrease in the transition T_ρ from ~215 to ~90 K. One of the possible explanations to this decrease in the resistive transition is the development of a mismatch between *A*- and *B*-sites as a result of *In* substations.

In some more details the replacement of Al^{3+} with ionic radius (0.535 Å) by In^{2+} with ionic radius (0.8 Å) at the *B*-site in the perovskite unit cell enhances the BO_6 octahedron and produces a long average *B*–O distance (this is confirmed from the calculation of the crystallographic parameters Table 4). This leads to a kind of distortion in this octahedron which enhances bending of the *B*–O–*B* bond. This, as expected will slow down the hopping process and weaken the ferromagnetic coupling between Mn^{3+} and Mn^{4+} ions over the octahedral *B*-site.

Fig. 8 illustrates the variation of ρ with temperature for $La_{0.7}\square_{\delta}Sr_{0.3-\delta}Mn_{0.96}In_{0.04x}Al_{(1-x)0.04}O_3$ perovskite system at zero magnetic field in the temperature range (300–400 K). The relation clearly shows that, for sample with $x=0.0$ ρ increases drastically with increasing temperature in a metallic behavior with positive temperature coefficient of resistivity (TCR) $[\partial\rho/\partial T>0]$. Metallic-to-semiconductor (MS) transition is occurred at ≈344 K with a sharp decrease in resistivity as temperature increased with a negative TRC $[\partial\rho/\partial T<0]$. As In replaces Al in this

Table 12
The transition temperature T, resistivity ρ, the reduced resistive and the activation energies for $La_{0.7}\square_{\delta}Ca_{0.3+\delta}Mn_{0.96}In_{0.04x}Al_{(1-x)0.04}O_3$

Sample	T_ρ (K)		T_ρ (K)	ρ (Ω cm)	$\Delta R(T)/R$	$E_{for\ semicon.}$ (eV)	$E_{for\ met}$ (eV)
	$T_{\rho c}$(K)	$T_{\rho h}$(K)					
$x = 0.0$	209	213	213	5	4.1×10^2	0.1229(2)	−0.0241(7)
$x = 0.2$	143	153	153	26	2.5×10^3	0.1440(3)	−0.0183(6)
$x = 0.4$	134	140	140	45	4.4×10^3	0.1297(2)	−0.0206(8)
$x = 0.6$	117	126	126	133	1.3×10^4	0.1373(9)	−0.0220(1)
$x = 0.8$	105	114	114	328	3.2×10^4	0.1364(4)	−0.0254(3)
$x = 1.0$	87	100	100	1477	1.6×10^5	0.1329(3)	−0.0142(4)

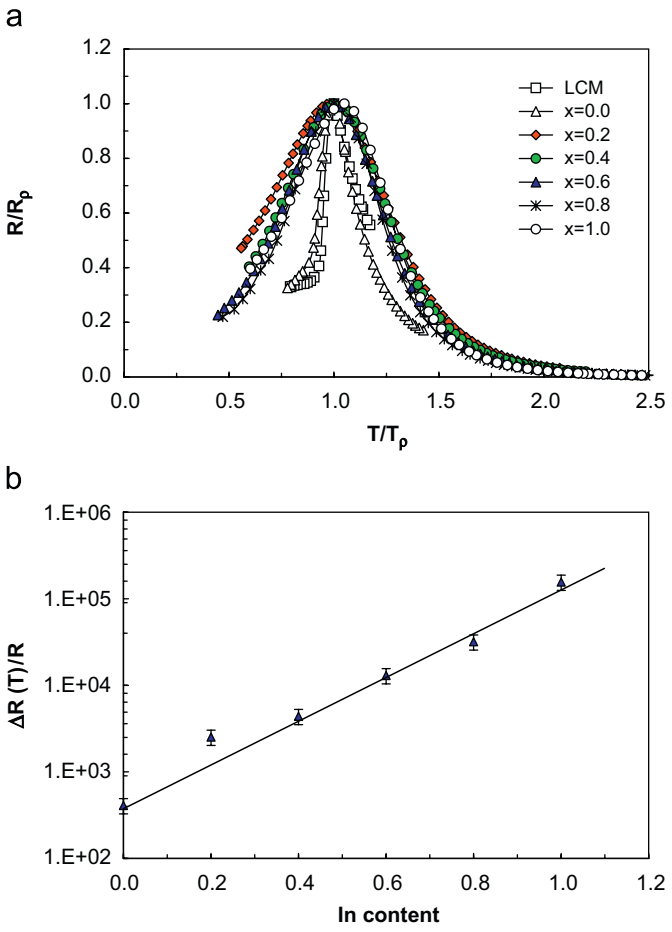

Fig. 7. (a) Dependence of the reduced resistivity $[R(T)/R(T_\rho)]$ vs. the reduced temperature $[T/T_\rho]$ for $La_{0.7}Ca_{0.3}MnO_3$ and Ca-series. (b) Variation of the amplitude of the giant resistive peak $\Delta R(T)/R = [R(T_\rho) - R(T_{288}K)]/R(T_{288}K)$ with In content x.

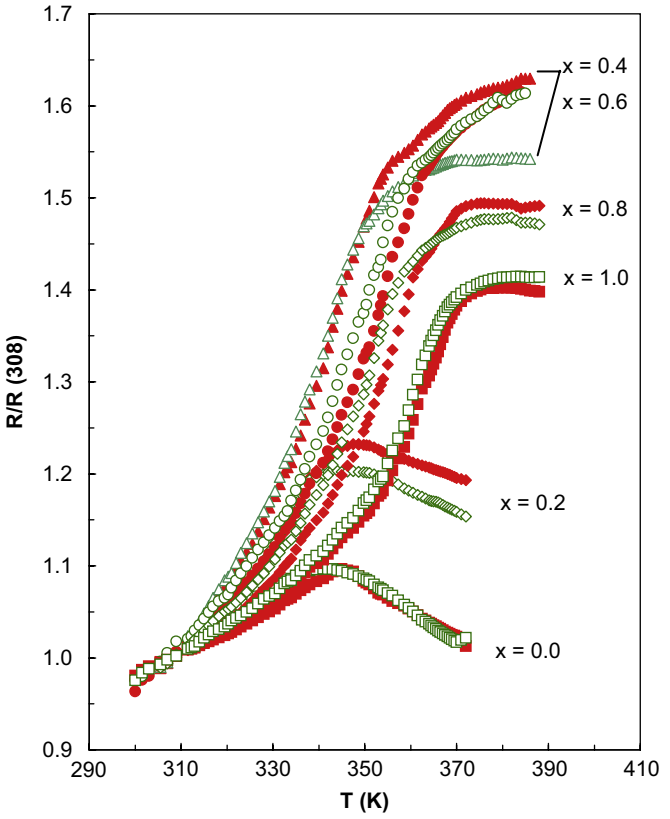

Fig. 8. Normalized $[R(T)/R(308)]$ resistivity versus temperature for $La_{0.7}\square_{\delta}Sr_{0.3-\delta}Mn_{0.96}(In_xAl_{(1-x)})_{0.04}O_3$ perovskite system at zero magnetic field in the range (300–400 K). Open symbol for cooling and closed symbol for heating.

unit cell the semiconducting behavior at the high-temperature range is decreased. The relation become flat with $[\partial\rho/\partial T \equiv 0]$ at $x = 1.0$ in this range of temperature.

The transition temperature T_ρ for Sr-series increases from $T_\rho \approx 341$ K at $x = 0.0$ to $T_\rho \approx 385$ K at $x = 1.0$ as In content x increased from $x = 0.0$ to 1.0. This is corresponding to the values of ρ at these maxima ranging from 0.27 to 0.14 Ω cm as listed in Table 13. The resistivity $\rho(T)$ curve displayed in Fig. 8 for this series measuring upon heating and cooling clearly demonstrates that there is a thermal hysteresis due to the first-order character of transition.

One of the possible explanation of the increase in T_ρ with In substitution, the effect of DE mechanism since it plays an important role between the Mn^{3+} and Mn^{4+} in CMR materials and in Sr-series in particular. For the parent manganite oxide $La_{0.7}Sr_{0.3}MnO_3$, Zener's DE mechanism [36] between the manganese and oxygen ions: Mn^{3+}–O–Mn^{4+} is most predominant and involves a transfer of an electron from the Mn^{3+} site to the intervening oxygen ion together with another simultaneous electron transfer from the oxygen ion to the Mn^{4+} site.

Table 13
The transition temperature T_ρ and activation energies of $La_{0.7}\square_\delta Sr_{0.3-\delta}Mn_{0.96}In_{0.04x}Al_{(1-x)0.04}O_3$ perovskite system

Sample	T_ρ (K)		ρ (Ω)	$E_{for\ semicon}$ (eV)	$E_{for\ met}$ (eV)
	$T_{\rho c}$	$T_{\rho h}$			
$x=0.0$	341	344	0.27	0.0332(1)	−0.0232(3)
$x=0.2$	351	354	0.12	0.0163(5)	−0.0575(4)
$x=0.4$	365	365	0.10	−0.0017(9)	−0.0625(7)
$x=0.6$	376	376	0.08	−0.0059(7)	−0.0491(9)
$x=0.8$	377	379	0.15	−0.0632(9)	−0.0423(7)
$x=1.0$	385	385	0.14	−0.0063(6)	−0.0396(2)

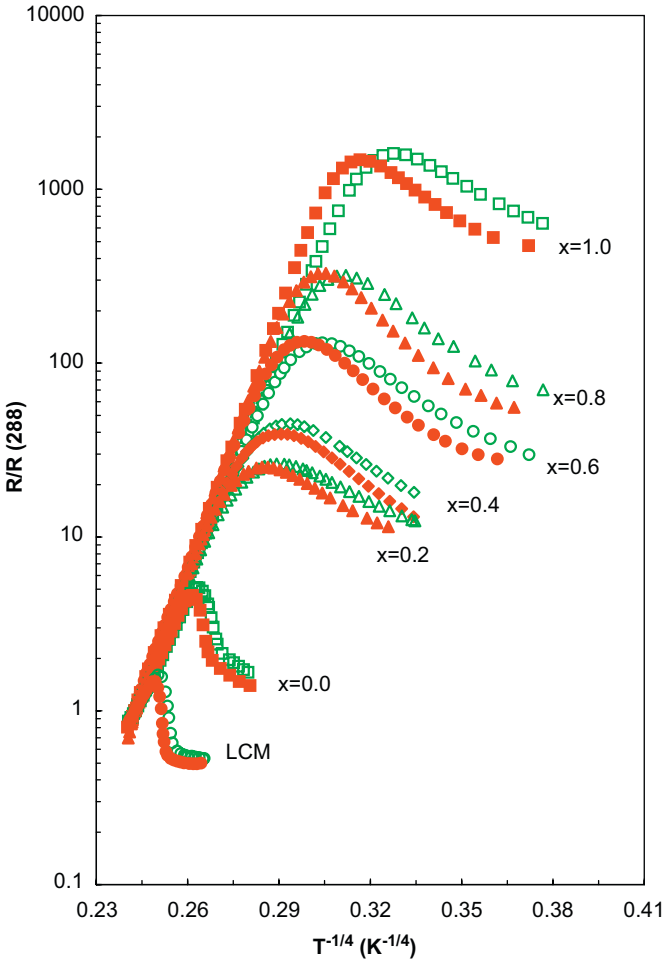

Fig. 9. Normalized $[R(T)/R(288)]$ resistivity versus temperature as $T^{-1/4}$ for $La_{0.7}\square_\delta Ca_{0.3+\delta}Mn_{0.96}(In_xAl_{(1-x)})_{0.04}O_3$ perovskite system at zero magnetic field in the range (50–300 K). Open symbol for cooling and closed symbol for heating.

Presence of very small concentration of Al (sample with $x=0.0$) in the present compounds influences the double exchange. This is because the nonmagnetic Al ion cannot participate in the double exchange: Mn^{3+}–O–Al^{3+} and thus act as a barrier to electron transport. Replacing Al by In in this series changes the Mn^{3+}/Mn^{4+} ratio. A linear

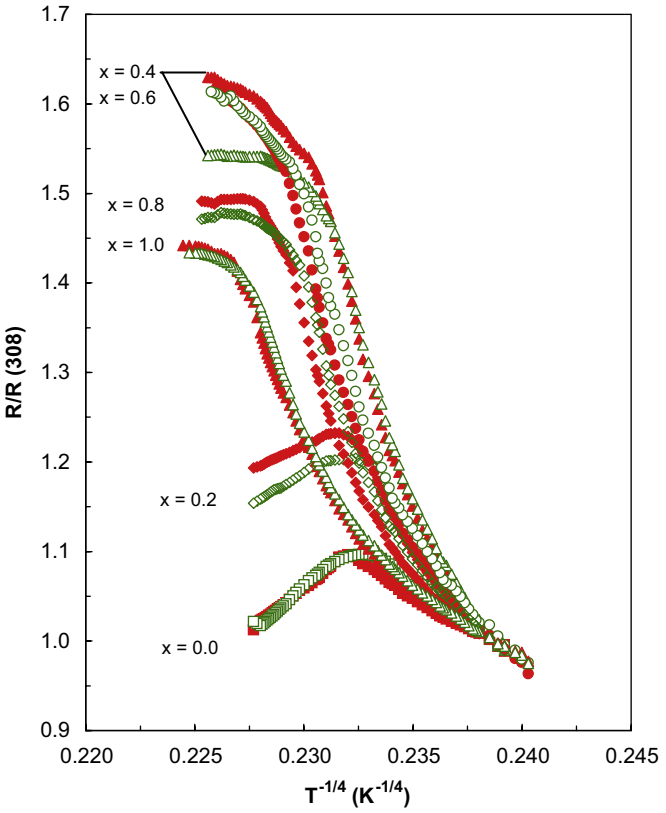

Fig. 10. Normalized $[R(T)/R(308)]$ resistivity versus temperature as $T^{-1/4}$ for $La_{0.7}\square_\delta Sr_{0.3-\delta}Mn_{0.96}(In_xAl_{(1-x)})_{0.04}O_3$ perovskite system at zero magnetic field in the range (300–400 K). Open symbol for cooling and closed symbol for heating.

decrease of Mn^{4+} with decreasing the nonmagnetic doping elements was previously reported [37–42].

In this regard, it is important to mention that, the Mn^{3+}/Mn^{4+} ratio is not the only factor that governs the variation of T_c in these compounds. Also, the variation of T_c cannot be explained in terms of DE interactions only. Definitely, there are other factors, which lead to the increase of T_c; such as the effect of the average ionic radius $\langle r_A \rangle$. In the present work the increase of T_c with increasing In content in (Sr-series) could be explained by the presence of a vacancy with average radius $\langle r_A \rangle \neq 0$ (as discussed above). This is in agreement with previously reported work [43,44].

For all samples, the resistivity above T_ρ fits the form

$$\rho = \rho_0 \exp(E_a/k_B T).$$

From which, activation energies E_a were found (see Tables 12 and 13). It is established that the zero-field resistivity data obtained for $T > T_\rho$ obey Mott variable range hopping (VRH) mechanism [35] when carriers are localized near the Fermi energy as in the case of hole-doped manganites.

Temperature dependence of ρ exhibits a universal behavior in this range

$$\rho = \rho_0 \exp(T/T_0)^{-1/4}, \quad (1)$$

$$T_0 = \beta/[k_B N(0) d^3].$$

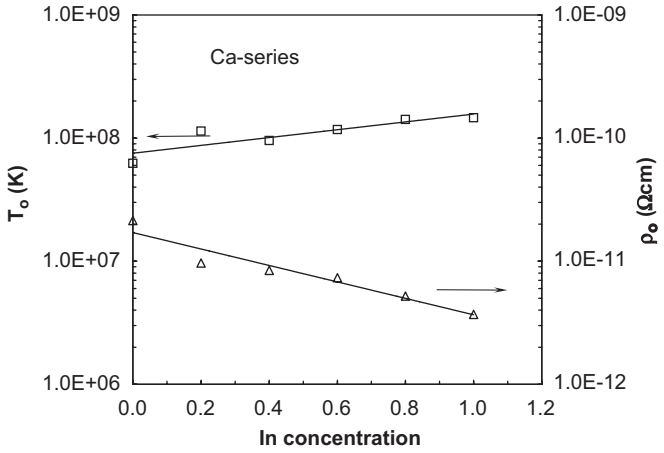

Fig. 11. ρ_0 and T_0 (in logarithmic scale) versus In content x at the range $T > T_\rho$ for $La_{0.7}\square_\delta Ca_{0.3+\delta}Mn_{0.96}(In_xAl_{(1-x)})_{0.04}O_3$.

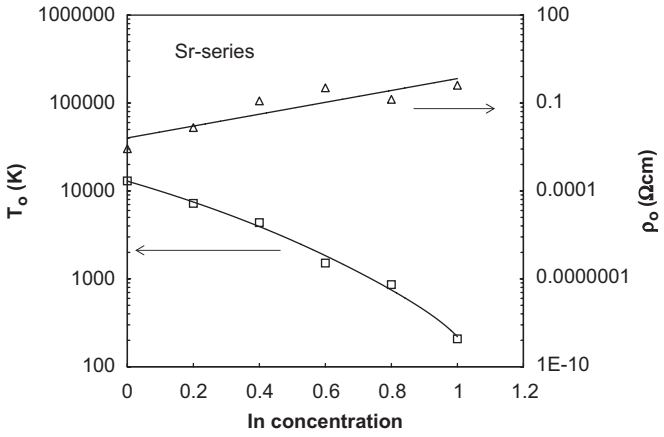

Fig. 12. Variation of ρ_0 and T_0 (in logarithmic scale) with In content x at $T > T_\rho$ for $La_{0.7}\square_\delta Sr_{0.3-\delta}Mn_{0.96}(In_xAl_{(1-x)})_{0.04}O_3$.

$N(0)$ is the density of states at the Fermi level, d is the localization radius of states near the Fermi level, k_B is the Boltzman constant, and β is numerical coefficient. In order to clarify this matter, the data of ρ versus temperature are re-plotted versus $T^{-1/4}$ in Figs. 9 and 10 for the Ca- and Sr-series. The fits of the data to the $T^{-1/4}$ dependence in the range of temperature $T > T_\rho$ for the present studied samples, indicate that such a behavior is typical for conduction by VRH between localized states. The fitting parameters ρ_0 and T_0 (Eq. (1)) for the resistivity governed by VRH conduction are plotted in a logarithmic scale in Figs. 11 and 12 for the Ca- and Sr-series, respectively.

Importance of MO_6 octahedra tilts in the distortion of RMO_3, oxides with perovskite structure has already been described [24,45]. The $\langle M\text{–O–}M\rangle$ bond angle is a measurement of the value of these tilts [46]. Moreover, in RMO_3 perovskite, the conduction bandwidth of $3d$ parentage is proportional to $\cos[180°-\langle M\text{–O–}M\rangle]$. So, the larger the $\langle M\text{–O–}M\rangle$ angle, the wider the conduction bandwidth [47–49]. Thus the conductivity behaviors are mainly brought about by the e_g bandwidth, the number of carriers and different localization effects (electron–electron correlation, structural disorder). In a simple electron gas approximation, $La_{0.7}Ca_{0.3}MnO_3$ is a system with a partially (or full) t_{2g} band and a partially (or full) e_g band in which the carriers varies down to a lower number due to both Al and In substitution for Mn in the octahedral B-site.

4. Conclusion

(Al and In)-doped La–Ca and La–Sr manganites series are synthesized in single-phase, orthorhombic with (space group *Pnma*) for La–Ca and rhombohedral with (space group $R\bar{3}C$) for La–Sr series. Determined lattice parameters of the two series show linear dependence with In content x. Solid solutions with replacement of Al and In for Mn with a full occupancies in the metal sublattices is confirmed from the refined atomic positions of the doped manganites, i.e. the (La + Ca or Sr) and (Mn + Al + In) occupancies both equal unity. Determined structural parameters show significant dependence on In content x. Resistivity measurements in zero field for the two series show metal-to-semiconducting transition. The transition temperature T_ρ has a strong dependence on the compositional parameter x.

References

[1] T.C. Gibb, J. Chem. Soc. Dalton Trans. (1983) 2031.
[2] Y. Zhuang, Y. Lin, D. Zhu, Y. Zheng, Z. Yu, J. Am. Ceram. Soc. 72 (1989) 1444.
[3] J. Hombo, Y. Matsumoto, T. Kawano, J. Solid State Chem. 84 (1990) 438.
[4] J.H. Choy, G. Demazeau, S.H. Byeon, Solid State Commun. 77 (1989) 649.
[5] K.S. Roh, K.H. Ryu, C.H. Yo, J. Solid State Chem. 142 (1999) 288.
[6] H.Y. Hwang, S.W. Cheong, R.G. Radaelli, M. Marwzo, B. Barlogg, Phys. Rev. Lett. 75 (1995) 914.
[7] F. Damay, A. Maignan, C. Martin, B. Raveau, J. Appl. Phys. 81 (1997) 1372.
[8] P.G. Radealli, G. Lannone, M. Marezio, H.Y. Hawang, S.W. Cheong, J.D. Jorgensen, D.N. Argyriou, Phys. Rev. B 56 (1997) 8265.
[9] A.J. Millis, P.B. Littlewood, B.I. Shraiman, Phys. Rev. Lett. 74 (1995) 5144.
[10] A.J. Millis, B.I. Shraiman, R. Mueller, Phys. Rev. Lett. 77 (1996) 175.
[11] L.M. Rodriguez-Martinez, J.P.A. Hfield, Phys. Rev. B 54 (1996) R15622.
[12] Y-u. Kwon, E-O. Chi, J-K. Kang, N.H. Hur, J. Appl. Phys. 82 (1997) 3072.
[13] P.A. Cox, Transition Metal Oxides, An Introduction to their Electronic Structure and Properties, Clarendon Press, Oxford, 1995.
[14] A.C. Larson, R.B. Von Dreele, Report LA-UR-86-784, Los Alamos National Laboratory, Los Alamos, NM, 1987.
[15] A.S. Wills, I.D. Brwon, "VaList," computer program, 1999 (from willsas@netscape.net).
[16] R.D. Shannon, Acta Crystallogr. A32 (1976) 751.
[17] B. Vertruyen, D. Flahaut, S. Hébert, A. Maignan, C. Martin, M. Hervieu, B. Raveau, J. Magn. Magn. Mater. 280 (2004) 75.
[18] V. Sedykh, V.Sh. Shekhtman, I.I. Zverkova, A.V. Dubovitskii, V.I. Kulakov, Physica C: Supercond. 433 (3–4) (2006) 189.

[19] S. Faaland, K.D. Knudsen, M.A. Einaesrud, L. RØrmark, R. Høer, T. Grande, J. Solid State Chem. 140 (1998) 320.
[20] M. Castellanos, A.R. West, J. Chem. Soc. Faraday Trans. 76 (1980) 2159.
[21] J.L. Garcia-Munuz, J. Fontcuberta, M. Suaaidi, X. Obradors, J. Phys.: Condens. Matter 8 (1996) L787.
[22] W. Archibald, J.S. Zhou, J.B. Goodenough, Phys. Rev. B 53 (1996) 4445.
[23] I.D. Brwon, Acta Crystallogr. B 48 (1992) 553.
[24] J. Pèrez-Cacho, J. Blasco, J. Garcia, R. Sanchez, J. Solid State Chem. 150 (2000) 145.
[25] G.H. Rao, K. Barner, I.D. Brown, J. Phys.: Condens. Matter 10 (1998) L757.
[26] A. Salinas-Sanchez, J.L. Garcia-Munoz, J. Rodriguez-Carvajal, R. Saez-Puche, J.L. Martinez, J. Solid State Chem. 100 (1992) 20.
[27] Z. Yang, L. Shaw, Nanostruct. Mater. 7 (1996) 873.
[28] L. Shaw, M. Zawrah, J. Villegas, H. Luo, D. Miracle, Metall. Mater. Trans. A 34 (2003) 159.
[29] G. Liu, S.C. Wang, W.P. Tong, M.L. Sui, J. Lu, K. Lu, Acta Mater. 44 (2001) 17.
[30] N.R. Tao, Z.B. Wang, W.P. Tong, M.L. Sui, J. Lu, K. Lu, Acta Mater. 50 (2002) 4603.
[31] H.J. Fecht, C. Moelle, In: S. Kornaneni, J.C. Parker, H.J. Wollenkerger (Eds.), Mater. Res. Soc. Symp. Proc. 457 (1997) 113.
[32] C.C. Koch, Nanostruct. Mater. 2 (1993) 109.
[33] F. Sánchez–Bajo, F.L. Cumbera, J. Appl. Crystallogr. 30 (1991) 427.
[34] R. Bathe, S.R. Shinde, K.M. Gapchup, K.P. Adhi, S.I. Patil, J. Magn. Magn. Mater. 256 (2003) 425.
[35] J.R. Sun, G.H. Rao, X.R. Gao, J.K. Liang, H.K. Wang, B.G. Shem, J. Appl. Phys. 85 (1999) 3619.
[36] Zener, Phys. Rev. 82 (3) (1951) 403.
[37] J.B. Goodenough, Phys. Rev. 100 (2) (1955) 564.
[38] E. Sotirova, X.L. Wang, J. Horvat, T. Silver, K. Konstantinov, H.K. Liu, Supercond. Sci. Technol. 15 (2002) 346.
[39] M.X. Xu, Z.K. Jiao, J. Mater. Sci. Lett. 18 (18) (1999) 1307.
[40] C. Zhu, R. Zheng, J. Phys.: Condens. Matter 11 (1999) 8505.
[41] V.P.S. Awana, E. Schmitt, E. Gmelin, A. Gupta, A. Sedky, A.V. Narlikar, O.F. de Lima, C.A. Cardiso, S.K. Malik, W.B. Yelon, J. Appl. Phys. 87 (9) (2000) 5034.
[42] W. Boujelben, A. Cheikh-Rouhou, J.C. Joubert, J. Solid State Chem. 156 (2001) 68.
[43] W. Boujelben, A. Cheikh-Rouhou, J.C. Joubert, Eur. Phys. J. B 24 (2001) 423.
[44] N.F. Mott, J. Non-Cryst. Solids 1 (1968) 1.
[45] A.M. Glazer, Acta Crystallogr. B 28 (1972) 3384;
A.M. Glazer, Acta Crystallogr. A31 (1975) 756.
[46] J.L. Garcia Muriez, J. Rodriguez Carvajal, P. Lacorre, J.B. Torrance, Phys. Rev. B 46 (1992) 4414.
[47] P. Lacorre, J.B. Torrance, J. Panetier, A.I. Nazzal, P.W. Wang, T.C. Huang, J. Solid State Chem. 91 (1991) 225.
[48] L. Syamaguchi, Y. Okimoto, Y. Tokura, Phys. Rev. B 54 (1996) R11022.
[49] J. Pèrez, J. Garcia, J. Stankiewicz, Phys. Rev. Lett. 80 (1998) 2401.